Master Thesis

Simulation of the Particle Distribution and Resulting Laser Processing of Selective Laser Melting Processes

by
Tobias Bode
Matriculation number: 2925670

Advisors: Dr.-Ing. Christian Weißenfels
M.Sc. Henning Wessels
Prof. Dr.-Ing. habil. Tarek I. Zohdi

1. Examiner: Prof. Dr.-Ing. habil. Dr. h.c. mult. Dr.-Ing. E.h. Peter Wriggers
2. Examiner: Dr.-Ing. Christian Weißenfels

25th of September, 2017

Prepared in the major of mechanical engineering at the institute for continuum mechanics (IKM) of the Leibniz University Hannover in cooperation with the laboratory of Prof. T.I. Zohdi at the University of California, Berkeley.

Master Thesis

Task definition for Tobias Bode, Matr.-Nr. 2925670

Topic

"Simulation of the Particle Distribution and Resulting Laser Processing of Selective Laser Melting Processes"

Objective and Task

Selective Laser Melting (SLM) is a 3D printing technology which is suited for additively manufacturing of metals and polymers. The main barriers of this process are the lack of reproducibility and the control of the influence of the process parameters, like laser power, scan rate, layer height and particle distribution for instance. A high fidelity simulation scheme for SLM processes can not only give an insight into the physical behaviour during the process, but can also help to control the whole 3D printing process in order to guarantee the reproducibility of the desired final product properties. However many challenges have to be overcome in order to guarantee a high fidelity simulation, like modelling the heat source or the phase change for instance. In this work the modelling of the heat source is addressed. A Ray Tracing algorithm should be implemented into the existing thermomechanical Optimal Transportation Meshfree (OTM) code. A Ray Tracing algorithm for the simulation of laser processes is investigated in combination with the Discrete Element Method in the literature. Therefore in a first step this algorithm should be recoded in order to benchmark the implemented Ray Tracing algorithm. In the next step this algorithm has to be implemented into the OTM code. An investigation by means of some examples should demonstrate the influence of the Ray Tracing algorithm on the fusion of two metal particles.

Declaration of Authorship

I hereby declare that the thesis submitted is my own unaided work. All direct or indirect sources used are acknowledged as references.

I am aware that the thesis in digital form can be examined for the use of unauthorized aid and in order to determine whether the thesis as a whole or parts incorporated in it may be deemed as plagiarism. For the comparison of my work with existing sources I agree that it shall be entered in a database where it shall also remain after examination, to enable comparison with future theses submitted. Further rights of reproduction and usage, however, are not granted here.

This paper was not previously presented to another examination board and has not been published.

Hannover, 25th of September, 2017 Tobias Bode

Contents

1 Introduction

The present thesis deals with the simulation of Selective Laser Melting (SLM)-processes. It shows some main simulation approaches and gives an introduction to the recent research in the continuum-based Optimal Transportation Meshfree (OTM)-Method. The coupling with the discretized Ray-Tracing heat source is developed and compared to the use and influence of volumetric heat sources in numerical examples. The integration of the Ray-Tracing algorithm in the OTM-Method opens up a large field of future research areas that are finally presented.

1.1 Motivation

In the following, the basics of the SLM are presented as a basis for the subsequent simulation. Selective Laser Melting is an additive manufacturing process, in which, layer for layer, a part is constructed out of metal powder. For each layer, the fine metal powder is distributed in the powder bed and a high power laser is used to melt and consolidate the powder. The SLM is a very flexible manufacturing technique that can produce components with a low rate of imperfections. The complex physical processes are not fully understood jet and the optimal process parameters are gained by experiments. To understand more physical phenomena involved in the SLM and to further optimize the properties of SLM produced parts, a preferably accurate simulation of the SLM processes is desirable. For recent researches see Zohdi (2014), King et al. (2015), Zohdi (2015a), Zohdi (2015b) and Ganeriwala and Zohdi (2016).

The following processing steps have to be considered by developing simulation models for SLM: First, the distribution of the particles in the powder bed has to be performed. For the simulation of a whole powder bed, a realistic particle distribution can be granted with the Discrete Element Method (DEM). If dealing with a small amount of particles, for example the melting of two particles, their positions can be set manually. As a second step, the heat input by the laser has to be modeled. Therefore, in the literature is a variety of volumetric and discretized laser models available, from which the most suitable for a specific simulation has to be selected while considering accuracy and computation time. Furthermore, the model of the heat transmission, and melting and consolidation of the particles is a very essential aspect. For investigations of a whole powder bed, the most commonly used method is the Discrete Element Method, due to its fast calculation of a large amount of particles. Nevertheless, a realistic and highly accurate simulation requires a continuum model that can reproduce the fusion of two single particles.

This is why, this thesis introduces to the continuum based OTM-Method which is able to simulate large deformations, which allows extensions for the most physical phenomena during the SLM as the melting of particles including latent heat, the surface tension, the consolidation and resulting internal stresses. Further extensions, like the partly evaporation of particles and the corresponding pressure, shall be made possible by the coupling with discretized heat sources. Besides, errors and instabilities that may occur due to inaccurate volumetric heat sources shall be reduced. Even if the presented method is more computationally intensive than other simulation approaches

discussed in the past research, it can help to understand the most important physical phenomena of SLM and may be used for a whole powder bed in the future, if the progress in computing power continues.

1.2 Objectives of this Work

The present thesis has the objective to analyze the effect of different heat sources to the Optimal Transportation Meshfree-Method. Especially, whether the above mentioned instabilities are due to the volumetric heat sources or if their inaccuracies are not the leading factor for the instabilities.

After an introduction to the different heat sources, the thesis presents the principle of the DEM, as it is a commonly used method for simulating SLM and can also be used to create a powder bed for the simulation with continuous methods. Hereinafter, the implicit thermo mechanical OTM-Method is introduced and a coupling between Ray-Tracing and the OTM-Method is developed. A criterion for the temporal discretization of the Ray-Tracing algorithm is presented and quantified with parameter studies.

Furthermore, the testing of the presented methods and algorithms is visualized and the outcome concerning the numerical instabilities is set out. Finally, there are suggestions for further research that is enforced due to the discretized heat source in the continuum based OTM-Method.

1.3 Theoretical Foundations

In the following, physical basics are listed which are the foundations for the derivation of the presented methods. For one thing, this basis is the balance of the linear momentum in the local form:

$$\rho \underline{\ddot{u}} = \operatorname{div} \underline{\underline{\sigma}} + \rho \underline{\bar{b}} \,, \tag{1}$$

with the density ρ, the acceleration $\underline{\ddot{u}}$, the Cauchy stress tensor $\underline{\underline{\sigma}}$ and the volume force $\underline{\bar{b}}$. The first law of thermodynamics states

$$\rho \dot{u} = \underline{\underline{\sigma}} : \underline{\underline{d}} - \operatorname{div} \underline{q} + \rho r \,, \tag{2}$$

where u is the specific inner energy, $\underline{\underline{\sigma}} : \underline{\underline{d}}$ is the inner stress power, $\underline{q}$ is the outgoing heat flow and r is the volume heat source. Combined with the second law of thermodynamics for reversible materials (which is justified by elastic solids and low viscous liquids)

$$D_{int} = \Theta \rho \dot{s} + \underline{\underline{\sigma}} : \underline{\underline{d}} - \rho \dot{u} = 0 \,, \tag{3}$$

with the dissipation power D_{int} and the entropy s, the local energy balance can also be written as

$$0 = -\Theta \rho \dot{s} - \operatorname{div} \underline{q} + \rho r \,. \tag{4}$$

This equation, together with equation 1, build the basis for the following Discrete Element Method and for the Optimal Transportation Meshfree-Method, where the weak forms are used.

Furthermore, the temperature-dependent material properties are handled in both, the DEM and the OTM-Method, in the same way: By means of substance tables, the most material data can be linearized conditional on their temperature. In case of a phase transition, the latent heat needs to be considered. An easy way to implement this lies in a manipulation of the specific heat capacity as illustrated in figure 1. In a defined interval $\Delta\Theta$ around the melting and evaporation point Θ_{melt} and Θ_{vap}, the heat capacity of the adjacent temperatures is averaged and increased by the latent heat referred to the length of the temperature interval $\frac{\Delta Q_{melt}}{\Delta\Theta}$ or rather $\frac{\Delta Q_{vap}}{\Delta\Theta}$.

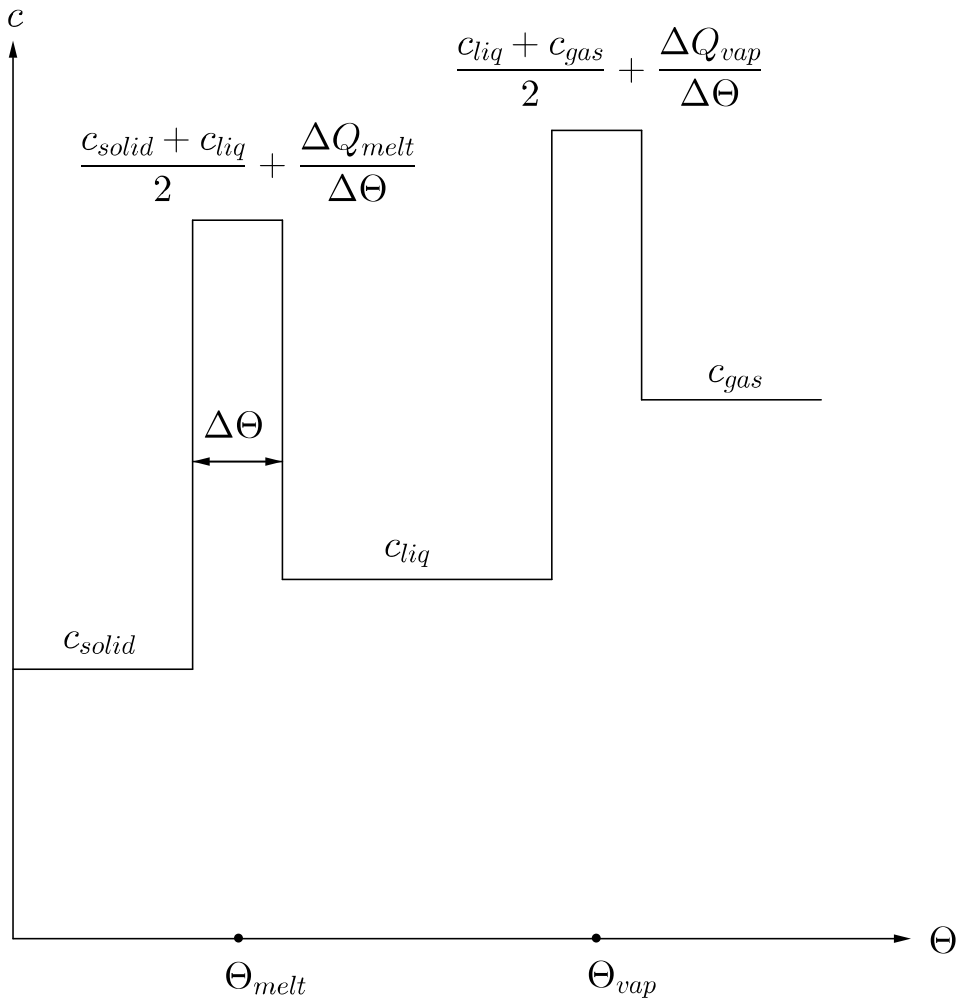

Figure 1 – Modeling of the latent heat using an increased heat capacity in an interval around the melting- and evaporation point

2 Heat Source Modeling

The heat source modeling is an essential issue in the simulation of selective laser melting. There are two general types to transfer the laser energy into the powder. In case of a simulation with discrete elements, the most often used models are the volumetric heat sources, where the laser power acting on a certain particle is computed from its position in the laser beam. The second main type of laser modeling lies in the discretization of the laser beam. A good overview of volumetric and discretized heat sources is presented in Zohdi (2014) and Zohdi (2015a).

Volumetric heat sources have their advantages generally in the reduced computational time, whereas discretized heat sources act on the particle's surface, hence they are able to display the partial heating and resulting evaporation of particles. A very accurate but CPU-intensive model is, to discretized the beam with the Maxwell's equations into its electric and magnetic field components. This small-scale field information is usually not necessary as the laser wavelength is much smaller than the particle diameter. A good compromise between physical accuracy and computing time is the Ray-Tracing algorithm which is presented below, as well as a volumetric heat source, based on the Beer-Lambert equation.

2.1 Volumetric Gaussian Distributed Beer-Lambert Heat Source

The volumetric heat source used in this thesis is based on the Beer-Lambert equation, which distributes the laser energy depending on the penetration depth. In addition, a radial weighting is included as in Ganeriwala and Zohdi (2016). That makes the volumetric heat source to

$$r = \alpha P_{laser} \cdot I\left(r, z\right) \tag{5}$$

with the absorptivity coefficient α and the distribution

$$I\left(r, z\right) = I_z\left(z\right) \cdot I_r\left(r\right) . \tag{6}$$

The distribution along the penetration depth is calculated according to Beer-Lambert to

$$I_z\left(z\right) = \frac{e^{-\beta z}}{\int_0^D e^{-\beta z}\, dz} = \frac{e^{-\beta z}}{\frac{1}{\beta}\left(1 - e^{-\beta D}\right)} , \tag{7}$$

where

$$\beta = \frac{3\left(1-\epsilon\right)}{2\epsilon D} \tag{8}$$

is the optical extinction coefficient, ϵ is the powder bed porosity and D is the maximal penetration depth. The distribution is normalized, so that the integral of the penetration depth in the heat affected zone equals one. For the radial distribution a Gaussian distribution is used:

$$I_r(r) = \frac{e^{-2\frac{r^2}{R^2}}}{\int_0^R \int_0^{2\pi r} e^{-2\frac{r^2}{R^2}}\, d\Phi\, dr} = \frac{e^{-2\frac{r^2}{R^2}}}{\frac{\pi R^2}{2}\left(1 - e^{-2}\right)}, \tag{9}$$

with the laser beam radius R. The normalization ensures, that the whole laser power is focused inside the beam radius.

Due to the not fully filled heat affected zone there will be a lag in the total energy balance while handling curved surfaces as in SLM. A way to get the full heat input in a powder bed consists in the correction of the distribution depending on the discretized volume V_h^{HAZ} in the heat affected zone V^{HAZ} (Chiumenti et al., 2016):

$$I^{corr}(r, z) = \frac{V^{HAZ}}{V_h^{HAZ}} I(r, z) \ . \tag{10}$$

2.2 Discretized Ray-Tracing Heat Source

In the Ray-Tracing Algorithm (see also Zohdi (2013)) the laser beam is discretized into jets of randomly placed rays, while each ray is given a direction n_r, a velocity c and an amount of energy E_r, depending on its position in the circular focused beam. The ray's velocity does not need to be the speed of the light. It is possible to scale it by a factor k^{reduce} conditional on the diameter of the particles, the time increment of the heat transfer algorithm and the scale of the processed simulation area. This speed reduction of the rays enforces the use of larger time steps which results in a reduced computational time.

After each time step, the ray positions $\underline{x}_r$ are updated in accordance with their reduced velocity:

$$\underline{x}_r(t + \Delta t) = \underline{x}_r(t) + \frac{c}{k^{reduce}} \Delta t \tag{11}$$

with the light speed c. The new time step starts with a collision check which checks, if rays are going to be absorbed. The procedure of this absorption depends on the type of the absorber (discrete element or a material point), hence it will be described in the according chapters.

3 Discrete Element Method

The Discrete Element Method was developed by P.A. Cundall in 1971. It is a very stable explicit method which is particularly useful in simulating powders as used in SLM. This chapter first presents the mechanical DEM based on the Gear-Algorithm as described in PÖSCHEL AND SCHWAGER (2005). Then, the extension to a thermo mechanical model with a discretized heat source is presented. Finally, the effectiveness in simulating a large number of particles is demonstrated in two examples.

The Gear-Algorithm consists of a predictor step in which the expected particle positions are computed through a Taylor expansion. Then, the forces acting on the particles are calculated in their predicted positions. Subsequently, the positions are adjusted in a corrector step, depending on the affecting forces. Due to the predictor-corrector algorithm, the force computation which is particularly expensive - concerning the processing time - is only performed once per time step.

3.1 Predictor

In the following, the prediction of the position, rotation and their time derivatives of particle i, with $1 \leq i \leq n^p$ is described. Therefore, the Taylor series is built on the particles' current variables. Usually an expansion of fourth or fifth order is sufficient. The position of particle i is the result of

$$\underline{x}_i^{pr}(t+\Delta t) = \sum_{n=0}^{4} \frac{\underline{x}_i^{(n)}(t)\Delta t^n}{n!}\,, \tag{12}$$

where Δt is the time increment and $\underline{x}_i^{(n)}$ are the time derivatives of the current position. Analogously, the velocity and higher derivatives as well as the rotation and corresponding derivatives are computed:

$$\underline{\dot{x}}_i^{pr}(t+\Delta t) = \sum_{n=0}^{3} \frac{\underline{x}_i^{(n+1)}(t)\Delta t^n}{n!}\,, \tag{13}$$

$$\underline{\varphi}_i^{pr}(t+\Delta t) = \sum_{n=0}^{4} \frac{\underline{\varphi}_i^{(n)}(t)\Delta t^n}{n!}\,. \tag{14}$$

3.2 Force Computation

The following force computation is based on the predicted particle positions. For reasons of simplicity in this subsection the index $(...)^{pr}$ is omitted. Within this work, the walls are modeled with static particles. Hence, all contact forces are based on the collision of two spherical particles. These contacts are modeled analogously to figure 2 with nonlinear characteristic curves for spring and damping. In addition to the contact forces $\underline{F}_i^{cont}$, the gravitational force $\underline{F}_i^{grav}$ has to be added to yield the total force acting on a particle:

$$\underline{F}_i^{total} = \underline{F}_i^{cont} + \underline{F}_i^{grav}\,. \tag{15}$$

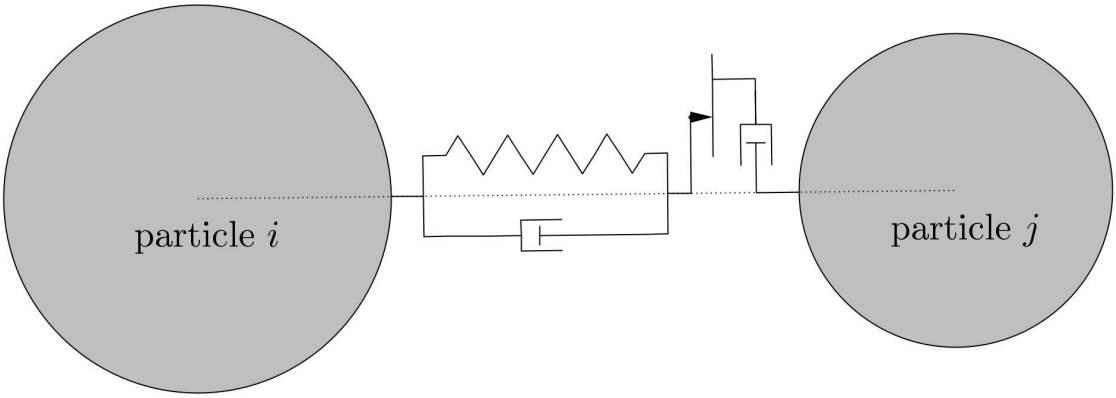

Figure 2 – Contact model of two spherical particles: normal spring-damper contact and tangential friction-limited damping contact

The contact force acting on particle i is assembled of the sum of the individual forces among the surrounding particles:

$$\underline{F}_i^{cont} = \sum_{\substack{j=1,\\ j\neq i}}^{n^p} \underline{F}_{ij}, \qquad \text{with} \qquad \underline{F}_{ij} = \begin{cases} \underline{F}_{ij}^{norm} + \underline{F}_{ij}^{tang}, & \text{for } \delta_{ij} > 0 \\ 0, & \text{for } \delta_{ij} \leqslant 0 \end{cases}, \tag{16}$$

where δ_{ij} is the mutual compression.

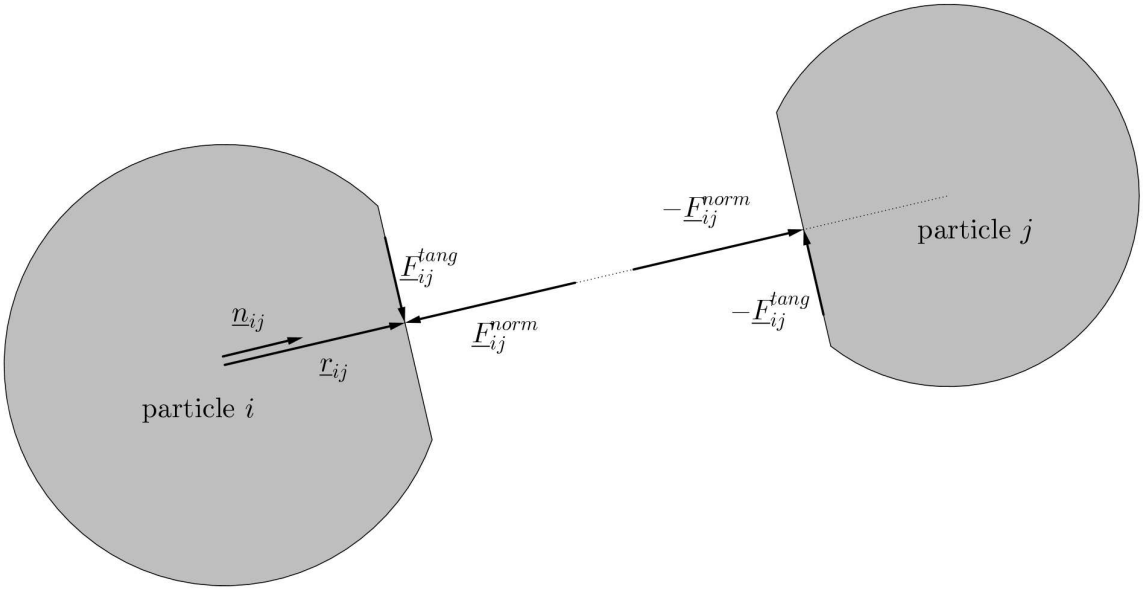

Figure 3 – Free body diagram of two colliding particles with acting normal and tangential forces

If two particles i and j are in contact, i.e. the mutual compression

$$\delta_{ij} = r_j + r_i - \left|\underline{x}_j - \underline{x}_i\right| > 0\,, \tag{17}$$

the contact force can be separated into a normal and a tangential part (figure 3). The tangential forces, resulting of the rough particle surface, act with a lever beam

$$\underline{r}_{ij} = \underbrace{\frac{\underline{x}_j - \underline{x}_i}{\left|\underline{x}_j - \underline{x}_i\right|}}_{\underline{n}_{ij}} \left(r_i + \frac{\delta_{ij}}{2}\right) \tag{18}$$

to the center of gravity on the particle. That yields to an angular momentum acting on the particle:

$$\underline{M}_i = \sum_{\substack{j=1,\\ j\neq i}}^{n^p} \underline{M}_{ij}, \qquad \text{with} \qquad \underline{M}_{ij} = \underline{r}_{ij} \times \underline{F}_{ij}^{tang}\,. \tag{19}$$

The normal force consists, as described in Ganeriwala and Zohdi (2016), of a spring and damper term:

$$\underline{F}_{ij}^{norm} = -\left(\frac{4}{3}\sqrt{r^{eff}}E^{eff}\delta_{ij}^{3/2} + d\dot{\delta_{ij}}\right)\cdot \underline{n}_{ij}\,, \tag{20}$$

with the effective radius and Young's modulus

$$r^{eff} = \frac{r_i \cdot r_j}{r_i + r_j} \qquad \text{and} \qquad E^{eff} = \frac{E_i \cdot E_j}{E_i\left(1-\nu_j^2\right) + E_j\left(1-\nu_i^2\right)}\,. \tag{21}$$

The damping coefficient can be modeled with the method of Wellmann and Wriggers (2012):

$$d = 2\zeta^{eff}\sqrt{2E^{eff}m^{eff}\sqrt{r^{eff}}}\cdot\delta_{ij}^{1/4}\,, \tag{22}$$

with the time derivative of the mutual compression

$$\dot{\delta}_{ij} = |\dot{\underline{\delta}_{ij}}| = \left(\underline{v}_i^{norm} - \underline{v}_j^{norm}\right)\cdot\underline{n}_{ij} \tag{23}$$

and a damping parameter that has to be set:

$$\zeta^{eff} = \frac{\zeta_i + \zeta_j}{2}\,, \tag{24}$$

whereby a damping parameter of $\zeta = 0$ stands for an elastic contact and a parameter of $\zeta = 1$ is a critically damped impact.
The tangential part of the particle contact force can be calculated as a relative-velocity dependent and against the relative-velocity pointed force, that is limited by the maximal transferable dynamic frictional force $\left|\underline{F}_{ij}^{norm}\right|\mu^{eff}$. That leads to

$$\underline{F}_{ij}^{tang} = \begin{cases} -\gamma^{eff}\cdot\underline{v}^{tang}, & \text{if } \left|\gamma^{eff}\cdot\underline{v}^{tang}\right| \leq \left|\underline{F}_{ij}^{norm}\right|\mu^{eff} \\ -\left|\underline{F}_{ij}^{norm}\right|\mu^{eff}\cdot\underline{t}_{ij}, & \text{else} \end{cases}, \tag{25}$$

with the effective sliding friction coefficient and damping constant

$$\gamma^{eff} = \min(\gamma_i, \gamma_j) \qquad \text{mit} \qquad \mu^{eff} = \min(\mu_i, \mu_j)\,. \tag{26}$$

Analogously to figure 4 the relative velocity $\underline{v}^{tang}$ can be calculated along the normal vector

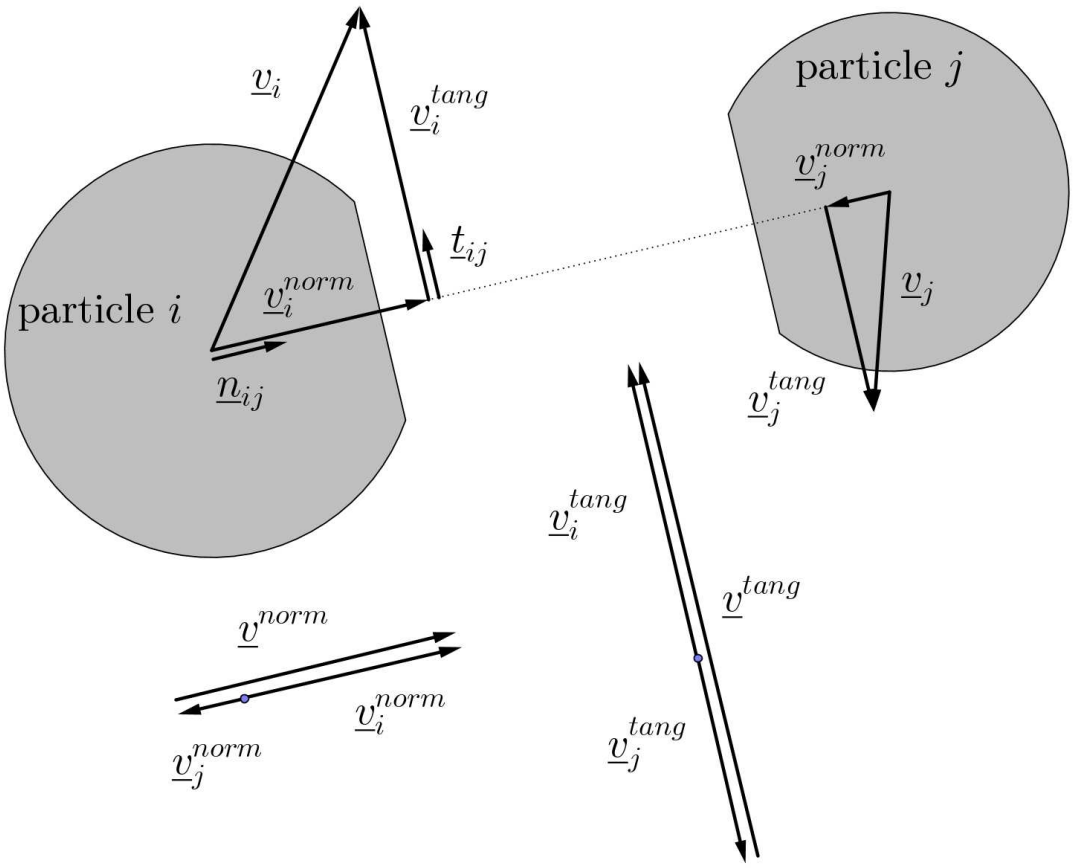

Figure 4 – Free body diagram with particle velocities separated in a normal and tangential component

$$\underline{t}_{ij} = \frac{\underline{v}^{tang}}{|\underline{v}^{tang}|} \tag{27}$$

to

$$\underline{v}^{tang} = \underline{v}_i^{tang} - \underline{v}_j^{tang} \,. \tag{28}$$

The particle velocity $\underline{v}_i$ can again be split in a normal and tangential component as follows:

$$\underline{v}_i = \underline{v}_i^{tang} + \underline{v}_i^{norm} \tag{29}$$

with

$$\underline{v}_i^{norm} = (\underline{v}_i \cdot \underline{n}_{ij})\underline{v}_i \qquad \text{and} \qquad \underline{v}_i^{tang} = \underline{v}_i - \underline{v}_i^{norm} \,. \tag{30}$$

3.3 Corrector

After the force computation the predicted kinematic variables can be corrected. This correction is based on the strong form of the principle of linear and angular momentum:

$$\underline{\ddot{x}}_i^{corr} = \frac{\underline{F}_i(\underline{x}_i^{pr}, \underline{\dot{x}}_i^{pr}, \underline{\dot{\varphi}}_i^{pr})}{m_i} \qquad \text{and} \qquad \underline{\ddot{\varphi}}_i^{corr} = \frac{\underline{M}_i(\underline{x}_i^{pr}, \underline{\dot{x}}_i^{pr}, \underline{\dot{\varphi}}_i^{pr})}{J_i}\,. \tag{31}$$

With the corrected particle acceleration a correction increment can be calculated as

$$\Delta\underline{\ddot{x}}_i = \underline{\ddot{x}}_i^{corr} - \underline{\ddot{x}}_i^{pr}\,. \tag{32}$$

The correction of the position, rotation and their derivatives is now computed as follows:

$$(\underline{x}_i^{corr})^{(\alpha)}(t+\Delta t) = (\underline{x}_i^{pr})^{(\alpha)}(t+\Delta t) + c_\alpha \frac{\alpha!}{\Delta t^\alpha}\frac{\Delta t^2}{2}\Delta\underline{\ddot{x}}_i\,, \tag{33}$$

whereby α is the time derivation order. For the rotational terms x can be replaced to ϕ. The constants c_α are in case of the Gear-algorithm of fifth order

$$c_0 = \frac{19}{90}, \quad c_1 = \frac{3}{4}, \quad c_2 = 1, \quad c_3 = \frac{1}{2} \quad \text{and} \quad c_4 = \frac{1}{12}\,. \tag{34}$$

Finally, the update of the particle variables has finished and can be repeated with the increased time

$$t \coloneqq t + \Delta t\,. \tag{35}$$

3.4 Thermal Extension Using the Ray Tracing Scheme

For the simulation of SLM the Discrete Element Method has to be extended by a thermal part. Therefore, the particles get a temperature as a primary variable and a temperature-dependent heat capacity. The heat transfer algorithm is staggered with the before introduced mechanical DEM. In this work, the ray tracing algorithm is used to model the laser beam. However, before the ray tracing algorithm for Discrete Elements is described, the basics of thermal transfer are presented.

In case of a Discrete Particle the strong form of the first law of thermodynamics (equation 4) can also be written as

$$m_i c_i \dot{\Theta}_i = \sum_{j=1}^{n^p} Q_{ij} + \sum_{r=1}^{n^r} H_{ir}\,. \tag{36}$$

Where m_i is the particle's mass, c_i its heat capacity, $\sum_{j=1}^{n^p} Q_{ij}$ is the incoming energy due to conduction and $\sum_{r=1}^{n^r} H_{ir}$ is the absorbed ray energy, i.e. the sum of

$$H_{ir} = E_{ir}^{inc} - E_r^{ref} = (1 - R_{ir})E_r^{inc}\,, \tag{37}$$

the differences of the incoming and reflected ray energies. The conduction between two touching particles can be modeled via Laplace's equation of heat transfer:

$$Q_{ij} = \begin{cases} K_{ij}A_{ij}\frac{\Theta_j - \Theta_i}{|\underline{x}_j - \underline{x}_i|}, & \text{for } \delta_{ij} > 0 \\ 0, & \text{for } \delta_{ij} \leq 0 \end{cases}, \tag{38}$$

whereby K_{ij} is the thermal conductivity and

$$A_{ij} = \pi \left(r_i^2 - l_i^2 \right) \tag{39}$$

is the contact area (see figure 5), with

$$l_i = \frac{1}{2} \left(\left| \underline{x}_j - \underline{x}_i \right| - \frac{r_j^2 - r_i^2}{\left| \underline{x}_j - \underline{x}_i \right|} \right) . \tag{40}$$

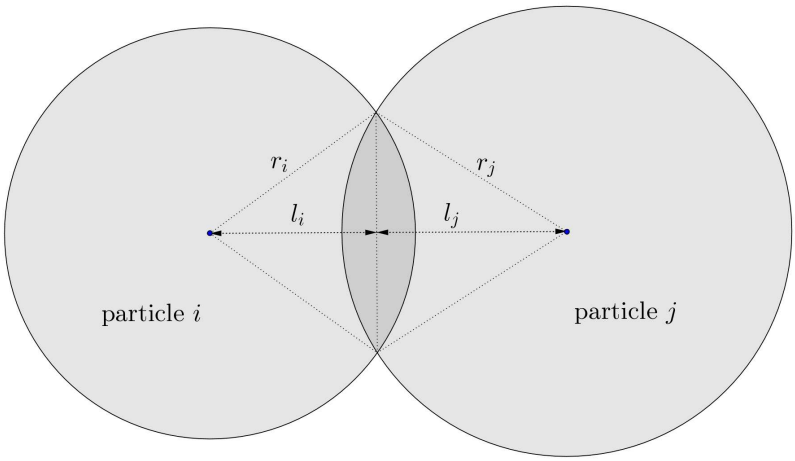

Figure 5 – Geometry of two particles in contact: The contact area A_{ij} is displayed in dark gray

Using the trapezoidal rule, the particle's temperature can be updated iteratively:

$$\Theta_i^{k+1}(t + \Delta t) = \Theta_i(t) + \frac{\dot{\Theta}_i(t)\Delta t + \dot{\Theta}_i^k(t + \Delta t)}{2} \Delta t \, . \tag{41}$$

The detection mechanism of rays is very simple. If a ray collides with a particle, it is partly absorbed and partly reflected depending on its angle of incidence. This yields the absorption condition

$$\left| \underline{x}_r - \underline{x}_i \right| \leq r_i \, , \tag{42}$$

where $\underline{x}_i$ is the position of the Discrete Element and r_i the particle radius. The reflection of a single ray at a particle surface is visualized in figure 6 and calculated as follows: $\underline{x}_r^{inc} = \underline{x}_r$ is the predicted position of the incoming ray, while $\underline{x}_r^c$ is the point of collision, i.e. the intersection point of the ray trajectory and the particle surface.

$$\underline{a}_r = \underline{x}_r^{inc} - \underline{x}_r^c \tag{43}$$

is the vector pointing from the collision point to the predicted ray position. To get the position of the reflected ray, this vector needs to be mirrored by the tangential plane

$$\underline{\underline{R}}_r = \underline{\underline{1}} - 2 \begin{pmatrix} {n_r^c}_x^2 & {n_r^c}_x {n_r^c}_y & {n_r^c}_x {n_r^c}_z \\ {n_r^c}_x {n_r^c}_y & {n_r^c}_y^2 & {n_r^c}_y {n_r^c}_z \\ {n_r^c}_x {n_r^c}_z & {n_r^c}_y {n_r^c}_z & {n_r^c}_z^2 \end{pmatrix} \tag{44}$$

that is defined by the normal vector of the particle surface in the point of collision

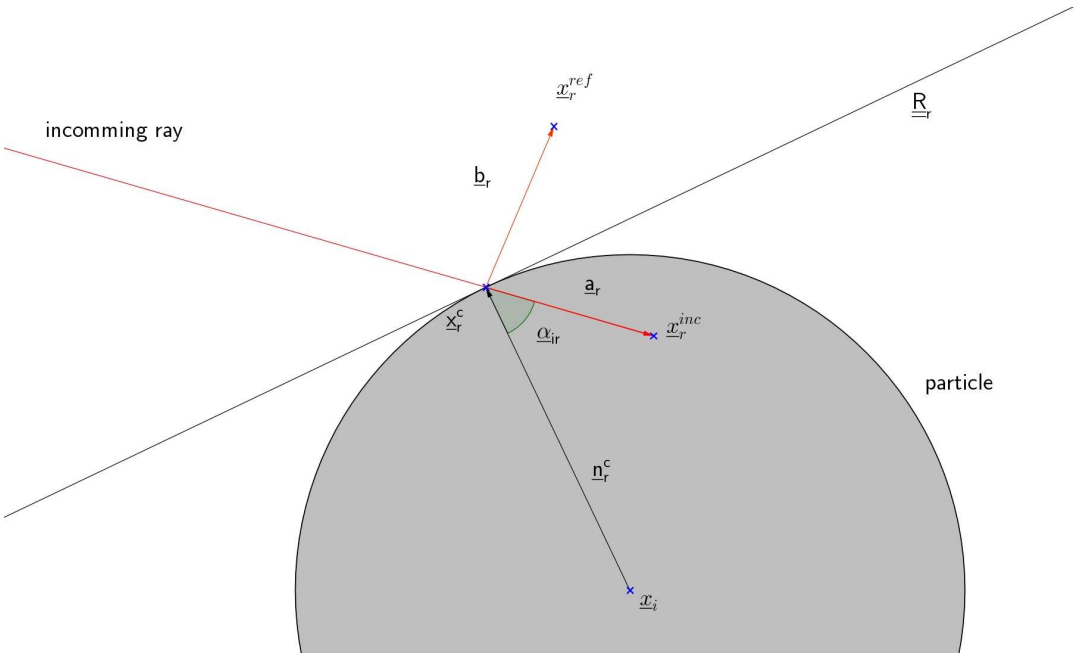

Figure 6 – Ray reflection on a spherical particle: The ray is reflected on the normal plane at the point of impact

$$\underline{n}_r^c = \frac{\underline{x}_r^c - \underline{x}_i}{|\underline{x}_r^c - \underline{x}_i|} \,. \tag{45}$$

The mirrored vector

$$\underline{b}_r = \underline{\underline{R}}_r \cdot \underline{a}_r \tag{46}$$

yields the position of the reflected ray

$$\underline{x}_r^{ref} = \underline{x}_r^c + \underline{b}_r \,. \tag{47}$$

The reflection ratio R_{ir} can be set to a global static parameter or calculated as a function of the incidence angle, the ratio of the refractive indexes and the ratio of the magnetic permeability (see Zohdi (2013)), where the incidence angle comes from

$$\alpha_{ir} = \left| \arccos\left(\frac{-\underline{a}_r \cdot \underline{n}_r^c}{|\underline{a}_r|\,|\underline{n}_r^c|} \right) \right| \,. \tag{48}$$

A possibility to reduce the computation time is to set a static absorptivity coefficient α like in volumetric heat sources, and to absorb the collided ray's energy multiplied with the absorptivity, neglecting the reflected part of the ray.

3.5 Example: Generating a Realistic Powder Distribution with DEM

For generating a realistic powder bed the commonly used method is mechanical DEM. There are two ways to do this: First, the particles can be pushed from the side into the powder bed, the second one is, to drop the particles with randomly assigned radii

using the Gaussian or probability distribution, and to run the Code until the particles get their equilibrium positions. In the following, an example for the second version is presented.

Using the probability distribution, particles with radii between $r_{min} = 60\ \mu m$ and $r_{max} = 70\ \mu m$ are systematically arranged in top of a cube that has an edge length of $1\ mm$. For processing the real material data of iron a low time step of $\Delta t = 10^{-8}\ s$ with a damping parameter of $\zeta = 0.7$ has to be used due to the high Young's modulus.

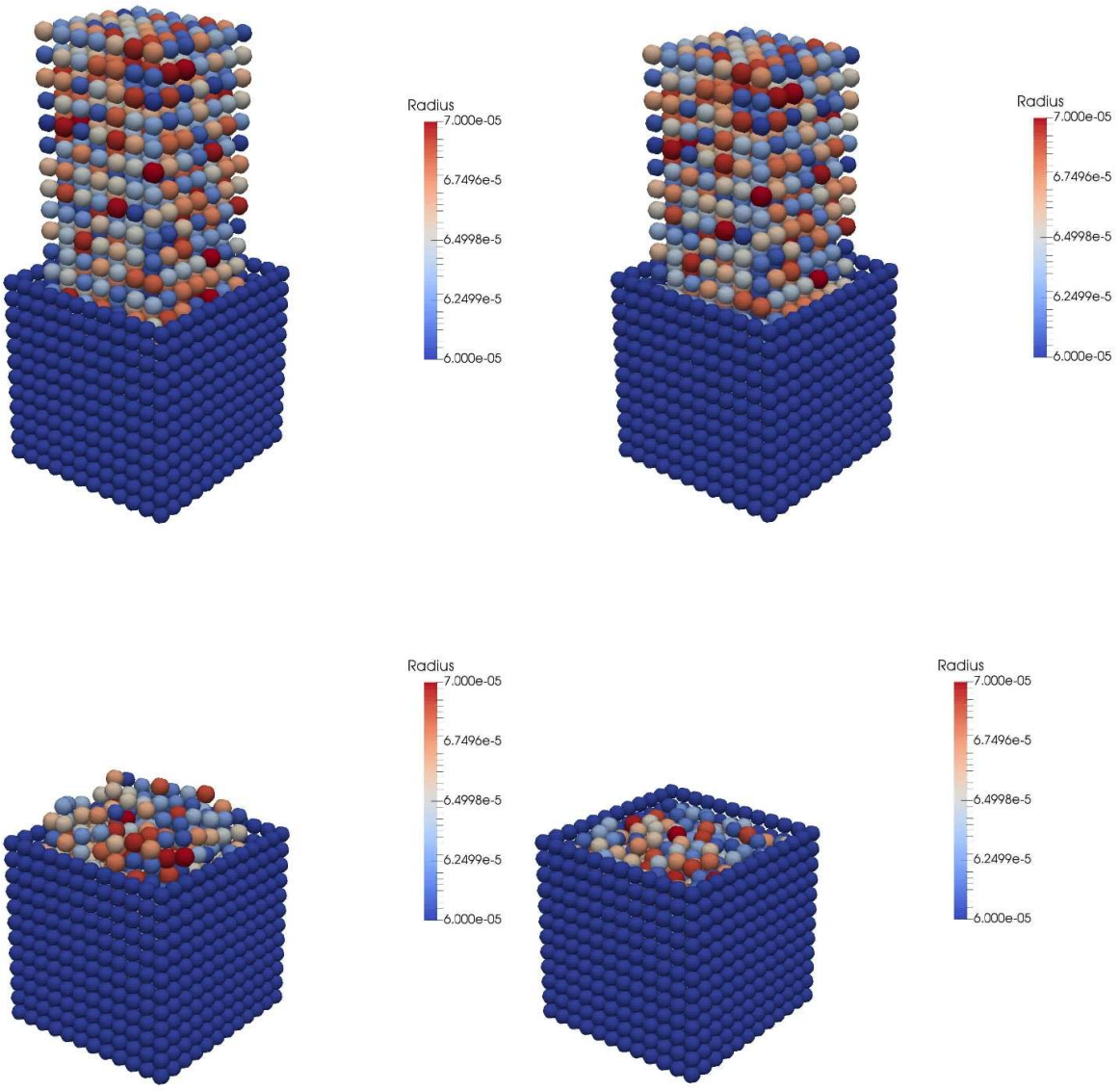

Figure 7 – Generating a natural particle distribution with the DEM, the probability distributed radii are visualized in different colors

Without a sorting algorithm as Link-cell or the Verlet approach, the code runs about three hours on a 24 CPU-cluster with Open Multi-processing (OpenMP) while simulating 1608 particles including wall particles. A sorting algorithm can reduce this time significantly. As pointed out in figure 7, a realistic particle distribution can be generated.

3.6 Example: Laser Processing of Discrete Particles

Once we have a realistic particle distribution in the powder bed, the subsequent laser processing can be started. To demonstrate the principle and mechanism of the simulation of laser processing of particles with the Ray-Tracing algorithm, the previously generated cube is heated with a laser pulse of 6000 $W \cdot 0.0006\ s = 3.6\ J$ of energy.

Note that in this example the particle positions are fixed and the heating is simulated only with a thermal code based on the first law of thermodynamics as described in subchapter 3.4. This simplification is reasonable for a demonstration and reduces the computing time. Nevertheless, for a more accurate simulation, the thermal and mechanical codes can be staggered and the material data linearized.

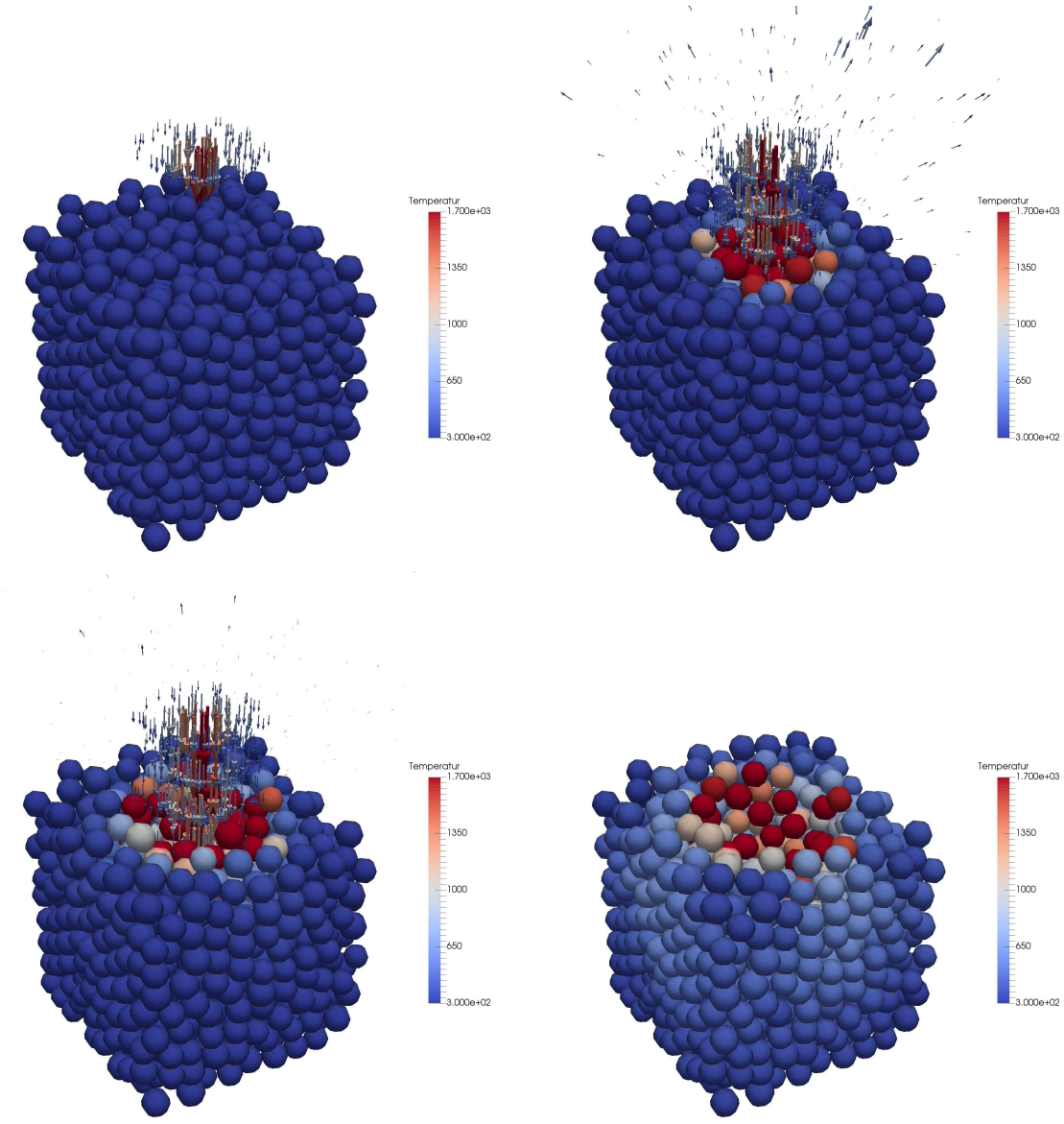

Figure 8 – Demonstration of the Ray-Tracing algorithm interacting with Discrete Elements in an only thermal code: Red particles are molten and deleted when vaporized

Figure 8 visualizes the simulation process. A circular focused laser beam with a power of 6000 W shoots a duration of 0.0006 s on the particle cluster. The impulse is discretized in a total number of 10000 rays. While the particles in the center of the beam instantly heat up, melt as described in chapter 1.3, and partly even vaporise - i.e. the Discrete Elements are deleted -, the particles that are not directly hit by rays warm up slower through heat conduction. For this demonstration, the magnetic permeability has been set to an arbitrary value of $\mu = 5\frac{Vs}{Am}$ for reasons of a good clarity of the reflection process of rays. With the real magnetic permeability for flat, shining iron, the reflection ratio is significantly higher, but that this value is also appropriate for powder is uncertain.

All in all, this only thermal example took about 80 s on four cores. The expansion on a staggered thermo mechanical code would not increase the computation time dramatically, because there occur just low and slow particle movements with a decreased Young's modulus of the heated material and therefore the time increment does not need to be reduced.

4 Optimal Transportation Meshfree-Method

The Optimal Transportation Meshfree-Method was introduced in Li et al. (2010). It is a meshfree method, based on the weak form of the Lagrangian formulation of the balance equations, which is supposed to be suited for fluid structure simulations. In this chapter, first the main principle of the thermo mechanical OTM-Method is presented. Then the coupling between the OTM-Method and the ray-tracing algorithm is developed. Subsequently, the ray-tracing parameters are optimized with parameter studies, and finally, some examples compare the ray-tracing scheme with volumetric heat sources.

4.1 Implicit Thermo Mechanical OTM-Method

The discretization in the OTM-Method is separated in two sorts of points: First, the nodal points, on which the primary variables (displacement $\underline{u}$ and temperature Θ) are defined, and second, the material points - also known as integration points - that are used to compute the stress $\underline{\underline{\sigma}}$, as well as the strain, heat flux, mass, density and volume. The linking between the different points is performed by a support domain, located around each material point, that finds surrounding nodal points (see figure 9). Hence, the number of nodal points can change and the resulting elements can overlap.

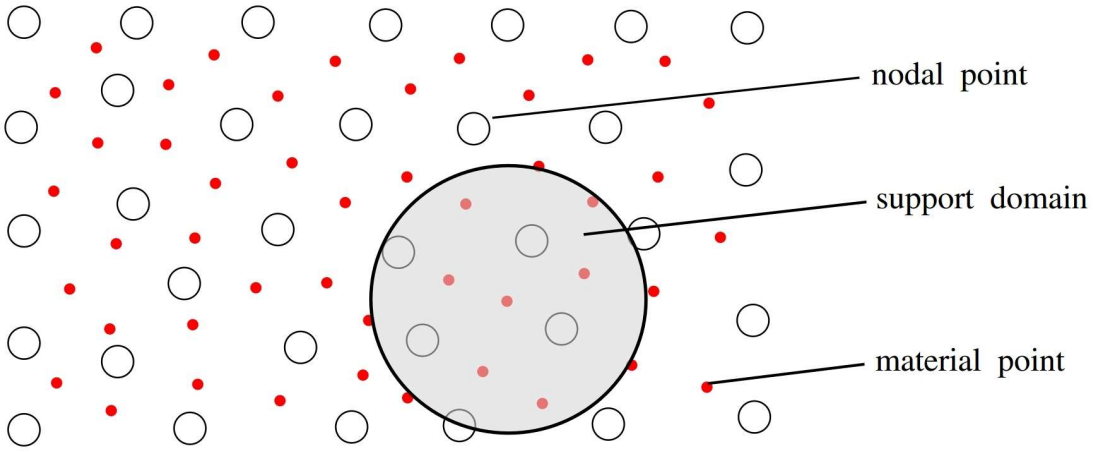

Figure 9 – Linking of material points and nodal points using a support domain: All contained nodal points are assigned to the material point of the support domain

Usually the Local Maximum Entropy (LME)-shape functions are used as shape functions, because of their flexibility in the number of nodes. Besides, there are some other types of shape functions, as the barycentric Mean Value shape functions.

Furthermore, the method is formulated in an incremental updating scheme, i.e. in each time step the positions are updated with an incremental deformation tensor. In this way, the volume fraction of each material point is updated with the determinant of the incremental deformation tensor. A more detailed overview of the mechanical OTM-Method can be found in Bode (2017).

The starting point are the balance equations, i.e. more precisely the weak forms of the linear momentum and the first law of thermodynamics. From the strong form of the linear momentum (equation 1), the weak form can be achieved through integration over the whole area, multiplication with a test function, partial integration and the usage of the divergence theorem to

$$+\int_v \rho\ddot{\underline{u}}\cdot\underline{\eta}\;dv-\int_a \underline{t}\cdot\underline{\eta}\;da+\int_v \underline{\underline{\sigma}}:\operatorname{grad}\underline{\eta}\;dv-\int_v \rho\overline{\underline{b}}\cdot\underline{\eta}\;dv=0\,. \tag{49}$$

The strong form of the first law of thermodynamics (equation 4) yields with the procedure above and the material model equation from Miehe (1988) for finite thermo elasticity

$$\rho\Theta\dot{s}=\frac{3\alpha K}{\rho_0}\ln J+(c+L_\Theta)\ln\frac{\Theta}{\Theta_0}\,, \tag{50}$$

to the weak form of the first law of thermodynamics

$$\begin{aligned}\int_v \frac{3\alpha K}{J}\Theta\operatorname{tr}\underline{\underline{d}}\;\delta\Theta\;dv+\int_v \rho\,(c+L_\Theta)\,\dot{\Theta}\delta\Theta\;dv+\int_a \delta\Theta\underline{q}\cdot\underline{n}\;da\\ +\int_v K\operatorname{grad}\Theta\operatorname{grad}\delta\Theta\;dv-\int_v \rho r\delta\Theta\;dv=0\,.\end{aligned} \tag{51}$$

Where the specific rate of heat flow can be gained through Fourier's equation for isotropic materials

$$\underline{q}=-K\operatorname{grad}\Theta\,, \tag{52}$$

where K is the thermal conductivity. As the stress tensor depends on the temperature, and the heat input in the first law of thermodynamics changes with the displacement, i.e. the weak forms are highly coupled, the balance equations can be staggered, or more accurate, processed with the Newton-Raphson algorithm. In this work, the multidimensional Newton-Raphson algorithm is used, which states

$$\begin{pmatrix}\underline{u}\\ \Theta\end{pmatrix}^{k+1}=\begin{pmatrix}\underline{u}\\ \Theta\end{pmatrix}^{k}-\underline{\underline{J}}^k(\underline{u},\Theta)^{-1}\begin{pmatrix}\underline{f}_{\underline{u}}(\underline{u},\Theta)\\ f_\Theta(\underline{u},\Theta)\end{pmatrix}^{k} \tag{53}$$

where k stands for the iteration step. In case of $k=0$, the primary variables $\underline{u}$ and Θ and all conditional terms are those from the old time step. Due to the dependency of the balance equations $\underline{f}_{\underline{u}}$ and f_Θ, the Jacobian's tensor generally has nonzero coupling terms:

$$\underline{\underline{J}}(\underline{u},\Theta)=\begin{pmatrix}\frac{\partial\underline{f}_{\underline{u}}}{\partial\underline{u}} & \frac{\partial\underline{f}_{\underline{u}}}{\partial\Theta}\\ \\ \frac{\partial f_\Theta}{\partial\underline{u}} & \frac{\partial f_\Theta}{\partial\Theta}\end{pmatrix}. \tag{54}$$

4.2 Coupling between Ray-Tracing and OTM-Method

An essential point in the coupling between discretized heat sources like ray-tracing and a continuum method lies in the detection mechanism of rays and in their absorption.

In this thesis, the rays are detected when entering a detection sphere of a material point (see figure 10), i.e. fulfill the condition of absorption

$$\left|\underline{x}_r - \underline{x}_p\right| \leq r^{det}\,, \tag{55}$$

with the distance between material point and ray $\left|\underline{x}_r - \underline{x}_p\right|$ and the detection sphere radius r^{det}.

In this work, in each time step, the position of the rays are updated with their direction and velocity, and the distances between each material point and every ray is checked. A further refinement would be to check only the material points at the surface. Therefore, a detection mechanism for the changing surface has to be found. A first approach consists in the mass gradient, which could also be used as a normal vector of a reflective surface to partly reflect the incoming rays, similar to the reflection on Discrete Elements in subchapter 3.4.

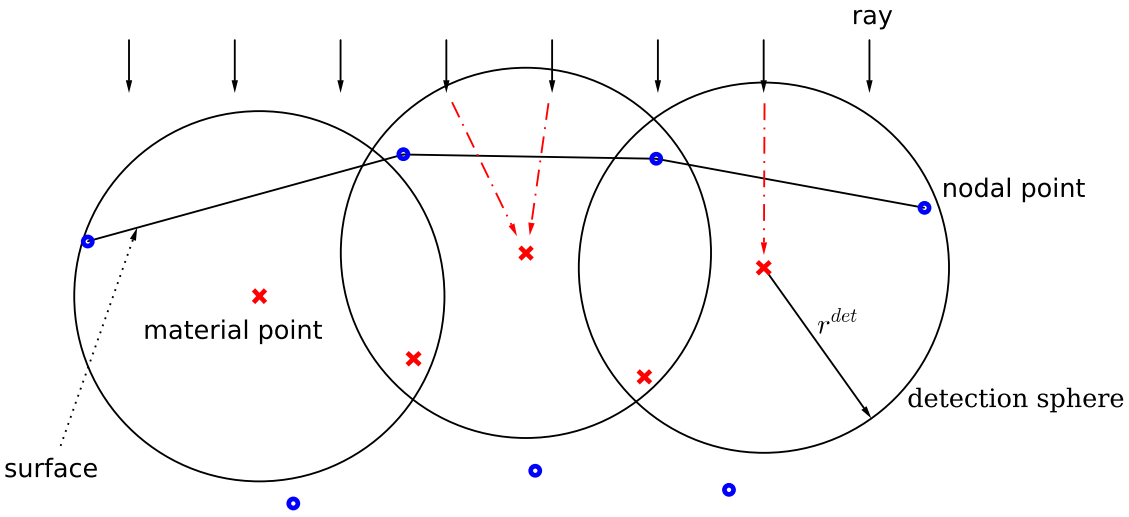

Figure 10 – Rays that are detected in a sphere around the material points are absorbed and treated as a volume power acting on the material point's volume

Here, a static reflection ratio $R_{ir} = 0.25$ is used and yields the summation of the absorbed energy at the material point in the current time step

$$H_{p\ n} = \sum_{\substack{r=1,\\ \text{collision}\overset{!}{=}true}}^{n^r} E_r^{inc}\,(1 - R_{ir})\ . \tag{56}$$

Referred to the time increment Δt, the absorbed energy is treated as a volume power in the weak form as follows:

$$\frac{E_{p\ n}^{abs}}{\Delta t^{sim}} = r_{p\ n}^{abs}\ v_{p\ n} = \frac{H_{p\ n}}{\Delta t^{sim}}\,. \tag{57}$$

4.3 Optimization of the Ray Discretization

In the following, the discretization of the laser beam is investigated through parameter studies and theoretical considerations. For the simulation, two particles with a diameter of 40 μm, lying on a 40 μm deep powder bed were heated from above with a 6 W-laser. For reasons of simplification, just the thermal routine was computed. While the spatial discretization, as well as the simulation time step $\Delta t_{sim} = 10^{-7}\ s$ was constant, the time step of ray-set creating and the number of rays in one set were varied. To find the best ray discretization, the consolidation time, the maximal occurred temperature and the CPU time are displayed along the ray discretization in figures 11 to 13.

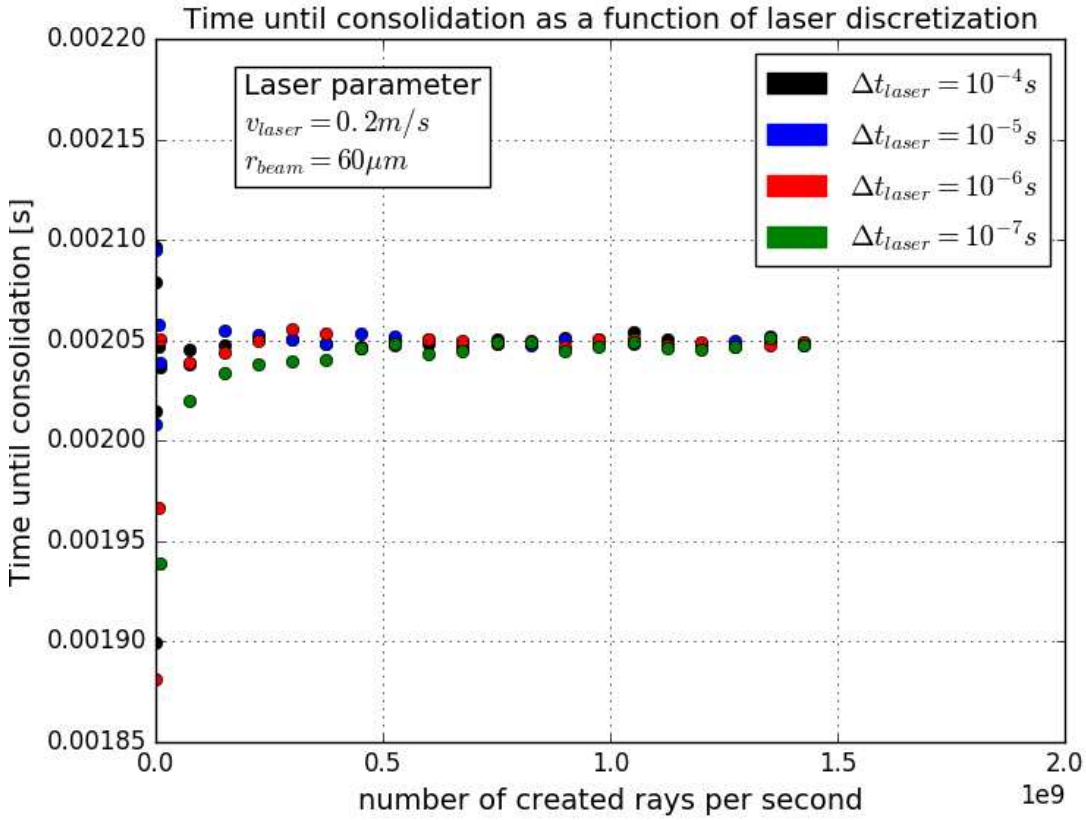

Figure 11 – The impact of the temporal ray-set discretization on the convergence of the consolidation time with an increasing number of created rays per second

Figure 11 shows, that the consolidation time converges independently from the ray-set creating time step with the number of created rays per second. From a number of $5 \cdot 10^8$ created rays per second, the relative deviation is just 0.5 %.

Note, that the maximal temperature that occurs during the simulation, which has an influence on the temperature distribution and the evaporation ratio, can change with bigger ray-creating time steps. That is because the maximal amount of energy, absorbed in one time step, increases with a rougher ray-set discretization:

$$\max(\Theta) \to \max\left(P_{p\ n}^{abs}\right) = \frac{\max\left(E_{p\ n}^{abs}\right)}{\Delta t_{sim}} \sim \frac{\overline{E}_r}{\Delta t_{sim}} = \frac{P_{Laser}\ \Delta t_{ray}}{\Delta t_{sim}} = \frac{\Delta t_{ray}}{\Delta t_{sim}} P_{Laser}\,. \quad (58)$$

The maximal temperature occurring in the simulation is located where the maximum in the heating power is located. That is the Energy absorbed by the material point p in time step n, divided by the simulation time step Δt_{sim}. The maximum of absorbed energy is proportional to the energy of each created ray set $\overline{E}_r = P_{Laser}\ \Delta t_{ray}$. Hence, the relation of the ray-set creating time step and the simulation time step has an influence on the maximal temperature. Figure 12 shows, that this relation has to be less than ten for a reasonable accuracy:

$$\frac{\Delta t_{ray}}{\Delta t_{sim}} \leq 10\,. \tag{59}$$

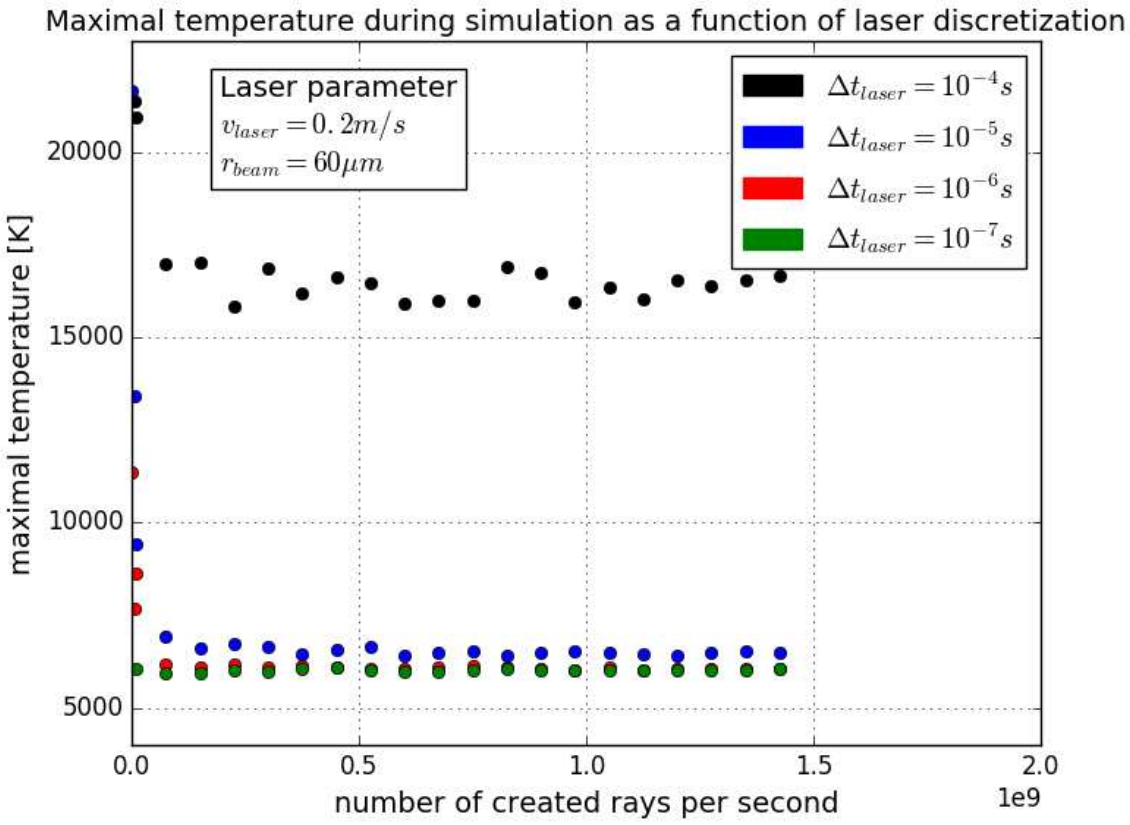

Figure 12 – The convergence of the maximal occurring temperature during the simulation depends on the temporal ray-set discretization

Further optimization of the beam discretization can be achieved in investigating the impact of the spatial discretization of the metal particles. As a finer discretization leads to lower mass fractions of the material points, the heating of a particular material point that absorbs a ray in a certain time step increases with a finer discretization. Hence, the maximal temperature during the simulation is not only proportional to the laser power, but also depends on the discretization, expressed by a parameter κ:

$$\max(\Theta) \sim \kappa\ P_{Laser}\,, \tag{60}$$

where κ is a function of the mean distance between two nearest rays in a set $\overline{d}_r$ and the mean distance between two nearest material points $\overline{d}_p$:

$$\kappa = \kappa\left(\overline{d}_r,\ \overline{d}_p\right) \ . \tag{61}$$

Further work is necessary to quantify this spatial discretization dependency.

By looking at the CPU time in figure 13, differences between time step of ray-set creating become evident. A number of $5 \cdot 10^8$ created rays per second costs an addition of about 20 to 25 % of CPU-time.

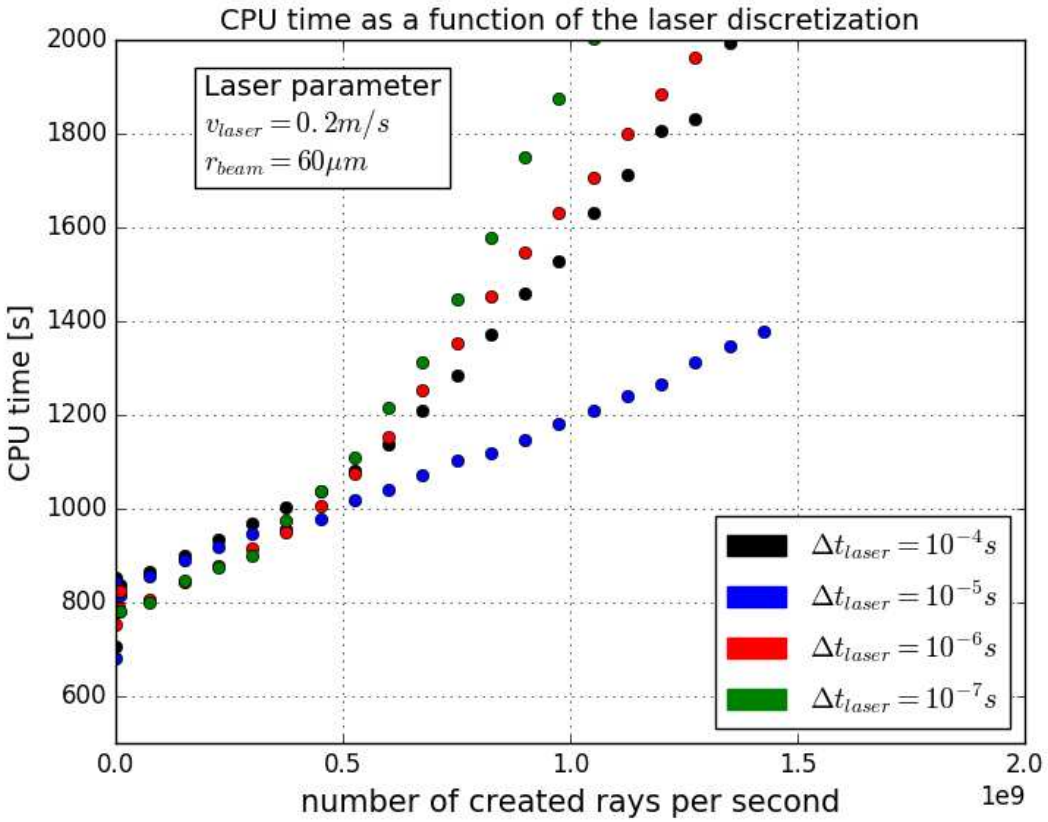

Figure 13 – The impact of the temporal ray-set discretization on the CPU time performance with an increasing number of created rays per second

If one uses less rays the code is faster in creating a small amount of rays in each time step, while for larger numbers of rays the computing time finds an optimum in creating ten times more rays in every tenth time step. In chapter 5 two approaches to lower the required laser discretization resolution and to reduce the discretization dependency between the Ray-Tracing algorithm and the OTM-Method are presented.

4.4 Example: Temperature Distribution with Volumetric and Discretized Heat Sources

The following comparison demonstrates the main advantages in using the Ray-Tracing algorithm. A single isolated metal particle is simulated with an only-thermal code while heating from the top with an laser pulse of 0.001 s with 0.6 W. For the reflection ratio, a static value of 0.25 is used. The absorbed energy is detected and with it the analytic equilibrium temperature is computed. In addition, the simulated end temperature and the maximal occurred temperature are recorded.

While with the Ray-Tracing heat source the full amount of energy - deducting the reflective part - gets into the particle, there is a lack of energy with the volumetric, Gaussian distributed Beer-Lambert heat source. In realistic powder bed simulations with a thermo-mechanical code this lack is even bigger. Nevertheless, based on equation 10, this lack can be fully adjusted (see table 1) even though this can cause problems when the laser enters or exits the powder bed.

	volumetric heat source without correction	volumetric heat source with correction	Ray-Tracing heat source
absorbed energy	$3.3307 \cdot 10^{-4}$ J	$4.5 \cdot 10^{-4}$ J	$4.5 \cdot 10^{-4}$ J
analytically computed end temperature	2247.4660 K	2931.1736 K	2931.1736 K
end temperature of simulation	2247.4647 K	2931.1719 K	2931.1736 K
maximal temperature during simulation	2361.2342 K	3084.8831 K	3778.6187 K

Table 1 – Heat sources in comparison: The maximal occurring temperature and the end temperature are heat source dependent

Despite the amount of absorbed energy, there is a difference in the temperature distribution during the heating process. In figure 14 the metal particle is displayed while warming on the left side with a volume-corrected, volumetric heat source and on the right side with discretized rays. The white material points have a temperature that is higher than the evaporation temperature. Apparently, the Ray-Tracing heat source leads to a heating starting at the surface where the laser beam hits the particle and thus can display a bigger temperature difference inside the particle. Hence, the Ray-Tracing scheme makes it possible to simulate the partially evaporation of metal particles and provides the basis for the inclusion of the physical phenomenon of the evaporation induced recoil pressure.

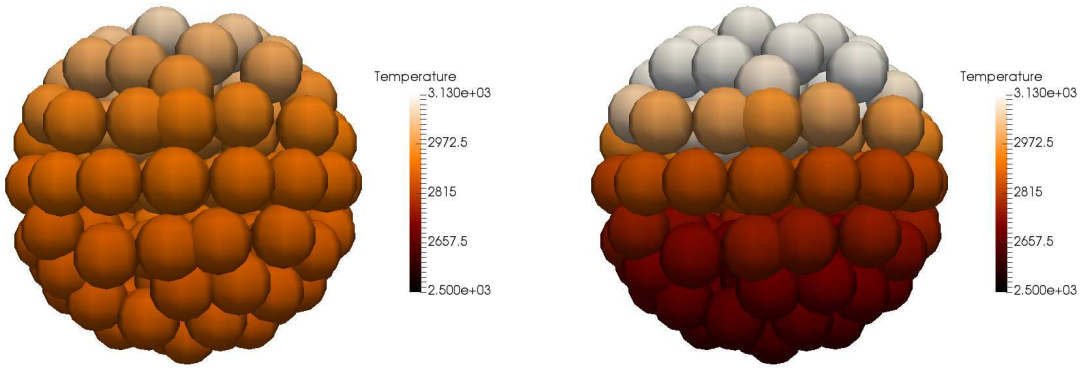

(a) Volumetric heat source with volume correction

(b) Discretized Ray-Tracing heat source

Figure 14 – The discretized Ray-Tracing heat source provides a differentiated temperature resolution at the particle scale

4.5 Example: The Laser Processing of Two Particles with Variable Laser Power

In the following subchapter, the fusion of two metal particles, lying on a solidified powder bed is simulated with changing laser powers. The particles are heated from left to right with a discretized laser beam (figure 15). At the bottom of the powder bed the nodes have Dirichlet boundary conditions of $\Theta = 300\ K$. The laser energy is transported by the rays to the surface of the particles, where they are absorbed when entering a detection sphere. The heat is transferred inside the particles through conduction, causing the particles to melt (white color). The surface tension leads to a fusion of the particles which consolidate while the heat is transfered into the powder bed.

On the left side of figure 16, the time until the last material point reaches the solidification temperature is plotted over the laser power. On the right side, the corresponding enlarge factor is displayed. This enlarge factor is a numerical parameter of the OTM-Method that controls the size of the support domain, and which is by default at 1.01 and is increased if the simulation fails.

The laser needs 0.0006 s to pass the two particles. That means, if time until consolidation is equal to 0.0006 s, there are no molten material points directly after the laser processing. With increasing laser power, the particles start to melt and they are still liquid after the laser irradiation. The higher the laser power is the more fully and the faster the metal particles melt. As a consequence, the contact between the particles and the powder bed increases, as figure 15 demonstrates, and the heat dissipation into the powder bed becomes stronger, so that the curves gradient decreases.

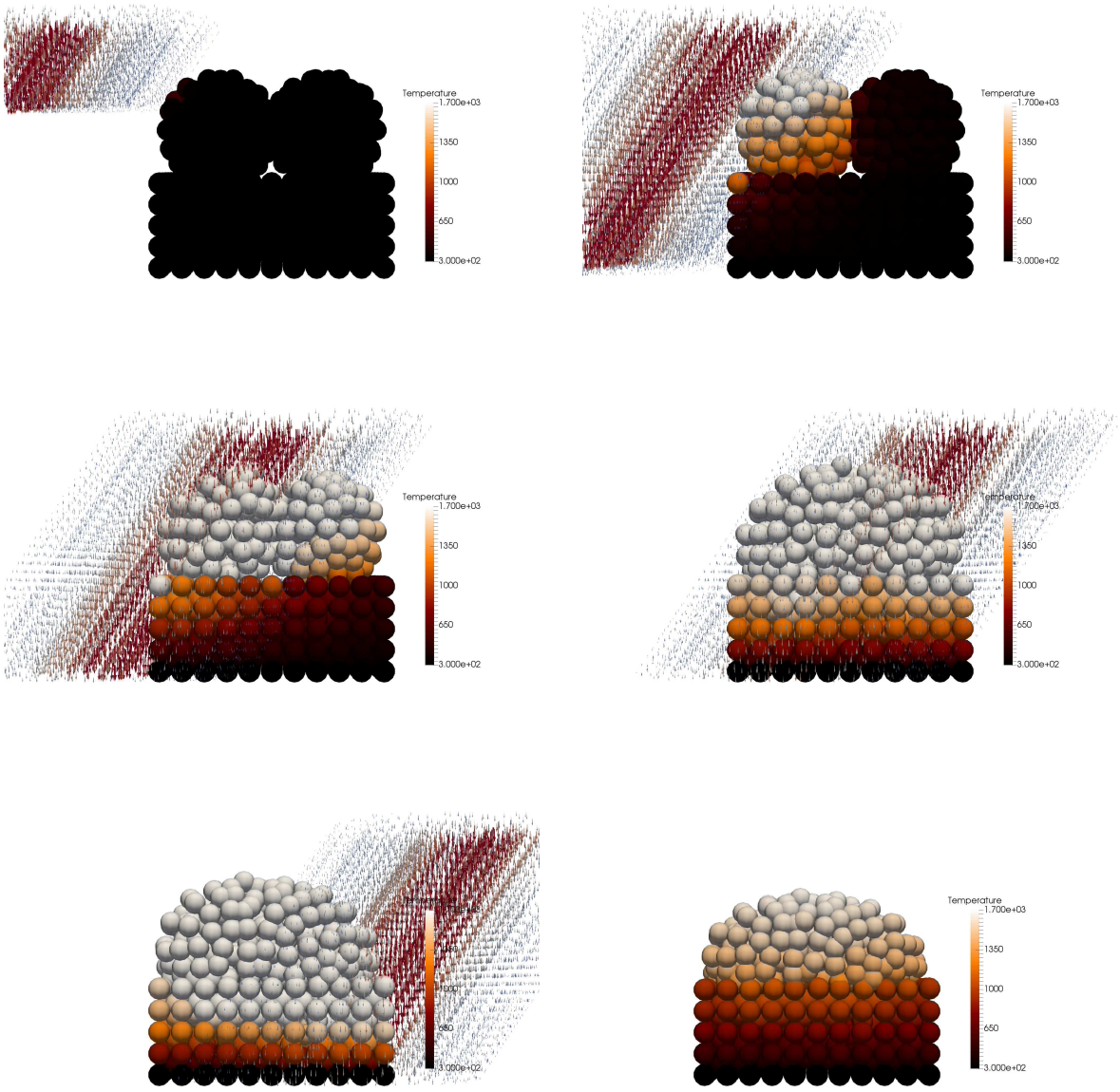

Figure 15 – The fusion of two particles simulated with the OTM-Method using a discretized laser beam

From a laser power of 9 W on, there appear instabilities in the consolidation time, that seem to have a connection to the changing enlarge factor. Nevertheless, these instabilities occur at a laser power where the two metal particles are already fully vaporized. In comparison to prior simulations with volumetric non volume-corrected heat sources, the simulation results are smoother and stable up to high laser powers. Though, the numerical instabilities indicates, that the OTM-Method has problems with changing enlarge factors. For the residual stresses the cooling to the ambient temperature is crucial. Investigations about the time that is needed to reach this temperature showed a significantly increased spattering in the cooling curve. This leads to the presumption that these problems are localized, inter alia, in the simulation of the heat transfer. The evidence for this is presented in chapter 5.

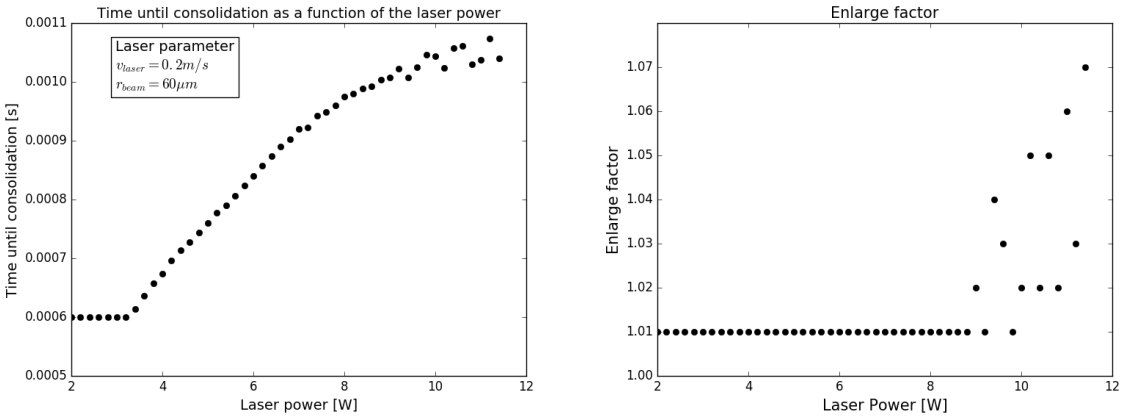

(a) Consolidation time **(b)** Enlarge factor

Figure 16 – Parameter study: The laser power is increased until the particles fully evaporate, the enlarge factor seems to have an impact on the instabilities at high laser powers

5 Summary and Extensions

In this last chapter, a review of the thesis and possible extensions are presented. The Selective Laser Melting is introduced in chapter 1 as an additive manufacturing process, in which layers of metal powder are melted together and build a 3D-part. In simulation approaches, on the one hand the metal powder and on the other hand the laser beam have to be modeled.

Starting with the momentum equation and the first law of thermodynamics, two general simulation concepts can be pursued. The Discrete Element Method is based on the strong form of these equations and is a very fast and relatively easy way to create realistic powder beds. The subsequent laser procession is less accurate, because the DEM can not display the realistic fusion of particles. If the simulation of melting pole is required, one has to switch to a continuum based method like the Optimal Transportation Meshfree-Method.

A further differentiation of possible simulation approaches consists in the modeling of the laser beam. Distinction can be made between volumetric and discretized heat sources. Whereas volumetric heat sources have their advantage in the computational time, discretized heat sources grant small scale field information and ensure that the temperature differences inside the metal particles can be grasped.

After the aforementioned methods were introduced, this thesis optimizes the Ray-Tracing scheme for the use in continuum based methods. Some of the possible applications are presented in numerical examples.

The optimization of the Ray-Tracing algorithm with respect to the time discretization in chapter 4.3 is based on parameter studies, whereas the effects of the spatial discretization are only based on theoretical considerations. In future, these proportionalities should be verified by profound simulations. A criterion for sufficient accuracy, like the relation of the mean ray distance and the mean material point distance $\frac{\bar{d}_r}{\bar{d}_p}$ shall be found and quantified. In addition, there is great potential in the research about the processing performance of the Ray-Tracing algorithm and the reduction of the discretization dependency between the laser and the particles.

For this purpose, two conceptual approaches are presented in figure 17. On the left side, the time time-dependent absorption of rays shall be smoothed through an aftermath of a ray detection. The energy of a detected ray has to be partitioned in the time step of detection and the following time steps. The figure on the right side of shows the distribution of a detected ray to surrounding material points that are located inside an influence domain of the detected ray. This technique shall achieve an independence in the spatial discretization of the laser and the processed particle.

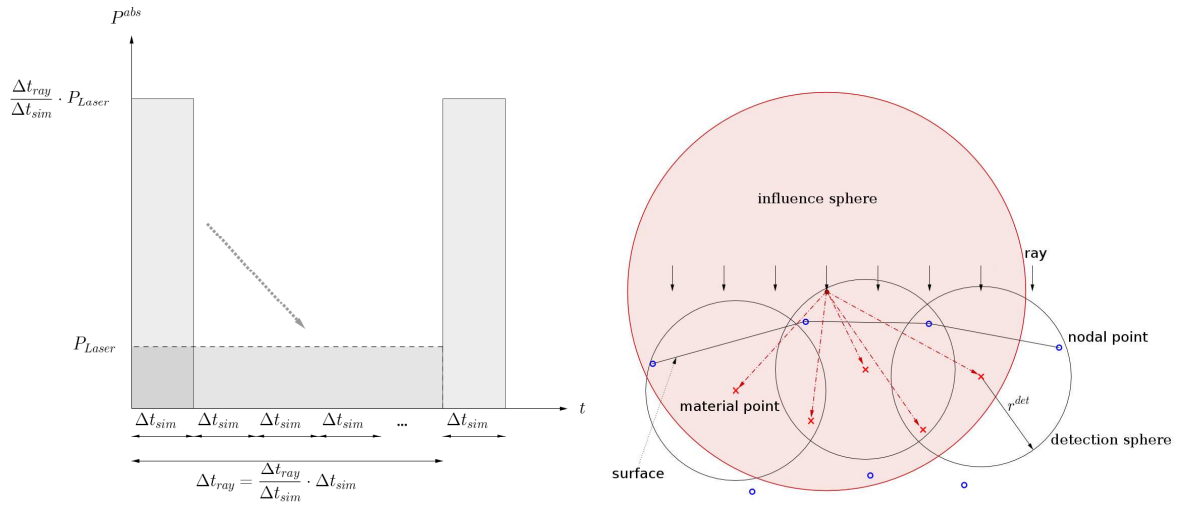

(a) Temporal Smoothing **(b)** Spatial Smoothing

Figure 17 – Conceptual approaches to reduce the computing time and the discretization dependency between the laser and the irradiated material

Furthermore, on the basis of the detailed temperature distribution inside the particles (see figure 14), which is due to the use of Ray-Tracing, the partly evaporation and the resulting recoil pressure can be considered. Advancement in this direction requires a stable simulation with higher laser powers and leads back to the investigation about the influence of the enlarge factor on the heat transfer mentioned in chapter 4.5.

The instabilities at high laser powers in figure 16 can be localized with the following example, where an isolated metal bloc is heated with a laser in an only thermal routine. The enlarge factor is varied and the maximal temperature as well as the time until the equilibrium position is reached is plotted for a volume-corrected volumetric heat source and the Ray-Tracing heat source in figure 18. Future examinations lead in the direction of the LME-shape functions.

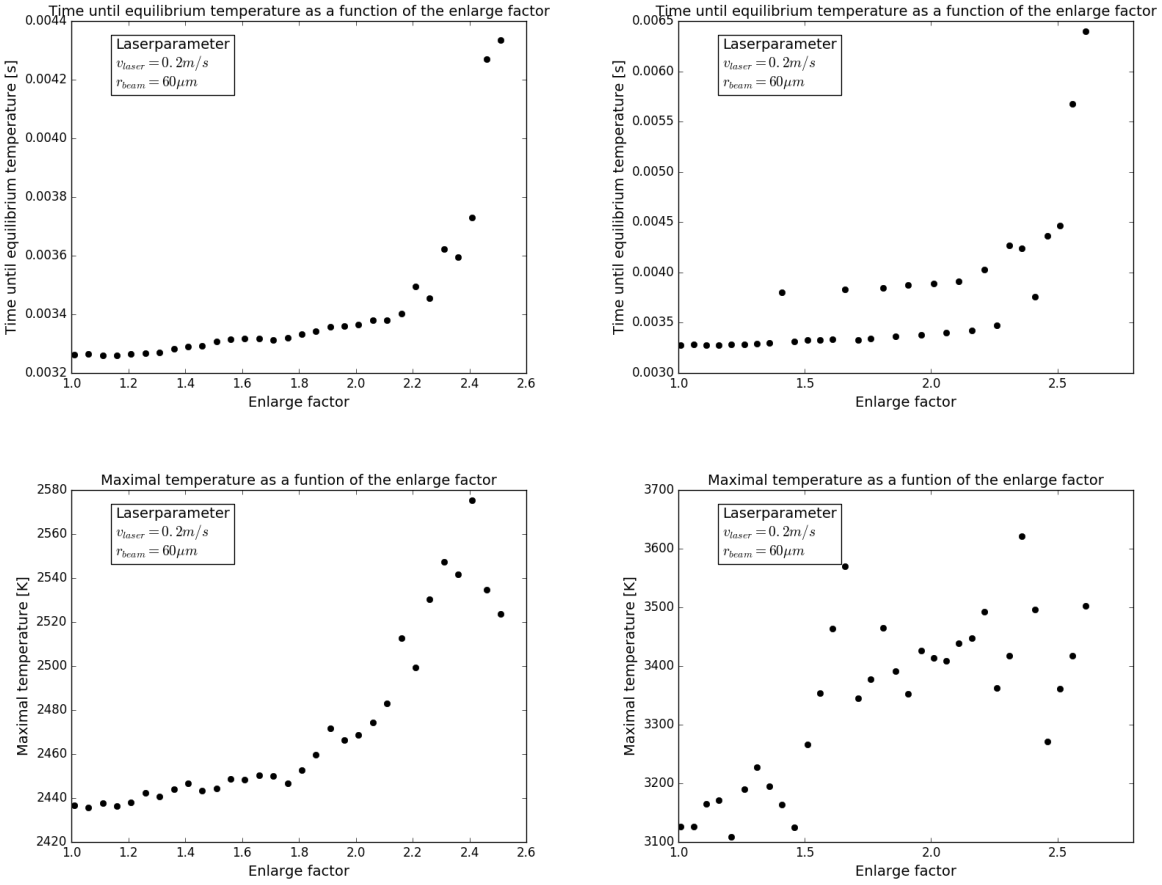

(c) Volumetric heat source with volume correction **(d)** Discretized Ray-Tracing heat source

Figure 18 – The simulation of the laser processing of a metal bloc with a thermal code shows that the enlarge factor has an influence on the heat transfer

List of Figures

List of Tables

References

Alkhaldi, H. (2007). *Contact Investigations of Granulat Mechanical Media in a Tumbling Sorting Machine*. PhD thesis, Universität Stuttgart.

Bode, T. (2017). Entwicklung einer netzfreien simulationsmethode auf basis der flexiblen elemente. Student research thesis.

Chiumenti, M., Cervera, M., Dialami, N., Wu, B., Jinwei, L., and c. Agelet de Saracibar (2016). Numerical modeling of the electron beam welding and its experimental validation. *Finite Elements in Analysis and Design*.

Ganeriwala, R. and Zohdi, T. (2016). A coupled discrete element-finite difference model of selective laser sintering. *Granular Matter*.

Habbal, F. (2009). *The Optimal Transportation Meshfree Method for General Fluid Flows and Strongly Coupled Fluid-Structure Interaction Problems*. PhD thesis, California Institute of Technology.

King, W., Anderson, A., Ferencz, R., Hodge, N., C.Kamath, Khairallah, S., and Rubenchik, A. (2015). Laser powder bed fusion additive manufacturing of metals; physics, computational and materials challenges. *Applied Physics Reviews*.

Li, B., Habbal, F., and Ortiz, M. (2010). Optimal transportation meshfree approximation schemes for fluid and plastic flows. *Numerical Methods in Engineering*.

Miehe, C. (1988). *Zur numerischen Behandlung thermomechanischer Prozesse*. PhD thesis, Universität Hannover.

Pöschel, T. and Schwager, T. (2005). *Computational Granular Dynamics - Models and Algrorithms*. Springer.

Rieger, A. (2002). *Adaptive Algorithmen für thermomechanisch gekoppelte Kontaktprobleme*. PhD thesis, Leibniz Universität Hannover.

Tavarez, F. and Plesha, M. (2006). Discrete element method for modelling solid and paritculate materials. *International Journal for Numerical Methods in Engineering*.

Wellmann, C. and Wriggers, P. (2012). A two-scale model of granular materials. *Comput. Methods Appl. Mech. Eng.*

Wessels, H. (2017). Thermomechanics. An introduction to the Implicit, Thermo-Mechanic OTM-Method.

Wessels, H., Gieseke, M., Weißenfels, C., Kaierle, S., Wriggers, P., and Overmeyer, L. (2017). Simulation von selective laser melting prozessen. *Additive Manufacturing Quantifiziert*.

Wriggers, P. (2001). *Nichtlineare Finite-Element-Methoden*. Springer.

Zohdi, T. (2013). Rapid simulation of laser processing of discrete particulate materials. *Arch Comput Methods*.

Zohdi, T. (2014). Additive particle deposition and selective laser processing - a computational manufacturing framework. *Comput Mech*.

Zohdi, T. (2015a). Modeling and simulation of laser processing of particulate-functionlized materials. *Arch Comput Methods*.

Zohdi, T. (2015b). On the thermal response of a surface deposited laser-irradiated powder particle. *CIRP Journal of Manufacturing Science and Technology*.